

## Inversion of helicopter electromagnetic data to a magnetic conductive layered earth

Haoping Huang\* and Douglas C. Fraser†

### ABSTRACT

Inversion of airborne electromagnetic (EM) data for a layered earth has been commonly performed under the assumption that the magnetic permeability of the layers is the same as that of free space. The resistivity inverted from helicopter EM data in this way is not reliable in highly magnetic areas because magnetic polarization currents occur in addition to conduction currents, causing the inverted resistivity to be erroneously high.

A new algorithm for inverting for the resistivity, magnetic permeability, and thickness of a layered model has been developed for a magnetic conductive layered earth. It is based on traditional inversion methodologies for solving nonlinear inverse problems and minimizes an objective function subject to fitting the data in a least-squares sense. Studies using synthetic helicopter

EM data indicate that the inversion technique is reasonably dependable and provides fast convergence. When six synthetic in-phase and quadrature data from three frequencies are used, the model parameters for two- and three-layer models are estimated to within a few percent of their true values after several iterations. The analysis of partial derivatives with respect to the model parameters contributes to a better understanding of the relative importance of the model parameters and the reliability of their determination.

The inversion algorithm is tested on field data obtained with a Dighem helicopter EM system at Mt. Milligan, British Columbia, Canada. The output magnetic susceptibility-depth section compares favorably with that of Zhang and Oldenburg who inverted for the susceptibility on the assumption that the resistivity distribution was known.

### INTRODUCTION

A number of interpretation methods exist for helicopter electromagnetic (EM) data that are designed to provide images that mimic the distribution of the true parameter(s) in the geologic section. Generally, the methods fall into two classes: (1) direct transform of data to a generalized model such as a half-space, and (2) inversion of data to a specific model such as a layered earth, where a starting model is employed, followed by iterative fitting of the data to yield a best fit in the least-squares sense.

Transform methods (e.g., Fraser, 1978; Huang and Fraser, 2001) have the advantage of yielding a single robust solution for the given output parameter, and the disadvantage that the output parameter may provide a poorly resolved image of the geology.

Inversion methods (e.g., Fitterman and Deszczpan, 1998; Sengpiel and Siemon, 2000) have the advantage of yielding a

much superior resolution for the given output parameter and the disadvantage that the output parameter may vary with the starting model, so this lack of robustness is always a concern when evaluating an interpretive output. The starting model is a common problem for all inversions and is not a topic of this paper. We use damped least-squares inversion based on singular value decomposition, where the starting model is determined directly from the resistivity-depth algorithm of Huang and Fraser (1996) and the apparent permeability algorithm of Huang and Fraser (2000), both of which are multi-frequency transforms from a half-space model. Sengpiel and Siemon (2000) show examples for determining starting models from transforms. Such starting models are often sufficient for a successful inversion of airborne EM data.

Inversion methods for the interpretation of electromagnetic (EM) data for a layered earth are being employed more commonly for helicopter-borne surveys as the data quality is improved and as both the number of frequencies and computer

Published on Geophysics Online January 30, 2003. Manuscript received by the Editor April 27, 2001; revised manuscript received December 2, 2002.

\*Formerly Geotrex-Dighem, Unit 2, 2270 Argentia Road, Mississauga, Ontario L5N 6A6, Canada; presently Geophex, Ltd., 605 Mercury Street, Raleigh, North Carolina 27603. E-mail: huang@geophex.com.

†Formerly Geotrex-Dighem, Unit 2, 2270 Argentia Road, Mississauga, Ontario L5N 6A6, Canada; presently consultant, 1294 Gatehouse Dr., Mississauga, Ontario L5H 1A5, Canada. E-mail: dougfraser1@cs.com.

© 2003 Society of Exploration Geophysicists. All rights reserved.

speed are increased. Numerous papers have been published on the methods used to invert for the resistivity of a layered earth model under the assumption that the magnetic permeability and dielectric permittivity are the same as those of free space (Holladay et al., 1986; Paterson and Reford, 1986; Huang and Palacky, 1991; Qian et al., 1997; Fitterman and Deszcz-Pan, 1998; Sengpiel and Siemon, 2000). However, EM data may be affected by the permeability in magnetic areas (Fraser, 1981; Huang and Fraser, 2000) which is the subject matter of this paper. EM data at frequencies above 10000 Hz may also be affected by the dielectric permittivity (Fraser et al., 1990; Huang and Fraser, 2002), but this is beyond the scope of this paper.

The resistivity derived from helicopter EM data, based on a nonmagnetic earth, is not reliable in highly magnetic areas because magnetic polarization currents occur in addition to conduction currents. The effect of a magnetic permeability  $\mu$  greater than the free space  $\mu_0$  is that the response at low frequencies may be dominated by a magnetization effect that is in-phase with, and in the same direction as, the primary field. As the frequency approaches zero, the in-phase response from a magnetic conductive earth becomes negative (in accordance with the normal signing convention) and frequency independent, and the quadrature response goes to zero. At higher frequencies, the magnetization effect and conductive effect are mixed, and the EM response becomes frequency dependent. The in-phase response is suppressed, although it may retain a positive value, and the positive quadrature response is increased. In this case, the magnetic effect on the data may go unnoticed, and an inversion can produce an overestimate, sometimes large, in the earth's resistivity when using a nonmagnetic earth model. See Beard and Nyquist (1998) for a discussion on the so-called in-phase shift due to magnetic polarization.

Magnetic permeability is one of the EM parameters of the earth. Ignoring it may not only cause the interpretation to be erroneous, but may also result in the loss of potentially useful information about the earth (Zhang and Oldenburg, 1999).

Some researchers have reported on the computation of magnetic permeability and resistivity from airborne EM data using noninversion methods. Lodha and West (1976) and Huang and Zhu (1984) presented methods for determining the magnetic susceptibility, conductivity, size, and depth of a magnetic conductive sphere in a dipole source field. Fraser (1973) described a technique for the estimation of the amount of magnetite contained in a nonconductive vertical dike. Fraser (1981) also presented a magnetite mapping method for helicopter EM systems, yielding the apparent weight-percent magnetite based on a nonconductive homogeneous half-space. He showed that a magnetite content of 0.25% can be recognized in the data. Huang and Fraser (2000) developed a resistivity and magnetic permeability mapping technique that yielded the relative magnetic permeability and resistivity of a magnetic conductive half-space.

Inversion of airborne multifrequency EM data for the magnetic permeability and resistivity of a layered earth has received limited attention. Beard and Nyquist (1998) inverted helicopter-borne EM data from five frequencies for a half-space resistivity and identified hazardous waste sites when magnetic permeability was included as an inversion parameter. Otherwise, the waste sites were almost invisible on a resistivity map. Zhang and Oldenburg (1997) describe a method to invert for the magnetic permeability of a layered earth under the

assumption that the resistivity distribution is known. The inversion technique may produce a good representation of the true magnetic susceptibility if the true conductivity-depth model is obtained by other methods. They also developed an inversion algorithm to simultaneously recover 1D distributions of electrical conductivity and magnetic permeability given the thickness of each layer (Zhang and Oldenburg, 1999).

In this paper, we invert for the magnetic permeability, resistivity, and thickness simultaneously for a layered earth under the quasi-static assumption that the dielectric permittivity is ignored. The inversion method is tested on synthetic data and on three-frequency data from a DigheM survey at Mt. Milligan, British Columbia, Canada. The results are compared to those obtained by Zhang and Oldenburg (1997).

The geometry of the problem is shown in Figure 1. The helicopter-borne transmitting and receiving coils, contained in a towed bird, are arranged in a horizontal coplanar orientation, although the change to a coaxial or to a vertical coplanar orientation is trivial. For purposes of an inversion, the sensor height  $h$  is assumed to be known from a radar or laser altimeter, and the dielectric permittivities are ignored for all layers. All synthetic examples shown below use a sensor height  $h$  of 30 m. The commonly transmitted DIGHEM system frequencies of 56000, 7200, and 900 Hz are used for the computation of the synthetic in-phase and quadrature components that in turn are used as input for the inversions.

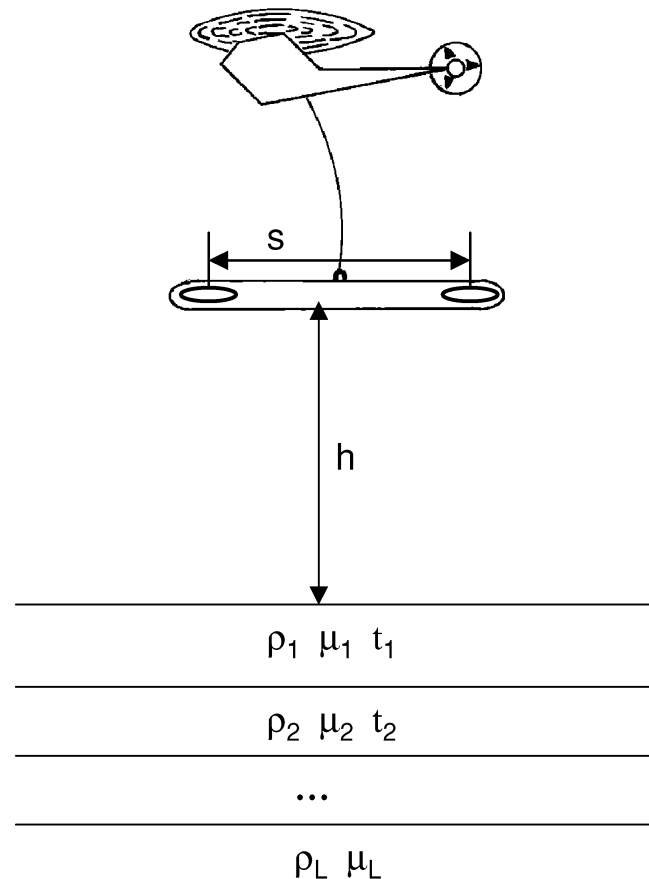


FIG. 1. The geometry of the EM coplanar coil system over a L-layer earth.

### THE FORWARD PROBLEM

The EM response of a layered half-space for dipole source excitation is given by Frischknecht (1967), Ward (1967), and Ward and Hohmann (1988), among many others. If a horizontal coplanar system is at a height  $h$  above the layered half-space, the secondary magnetic field  $H_s$ , normalized against the primary field  $H_0$  at the receiving coil, is

$$\frac{H_s}{H_0} = s^3 \int_0^\infty R(\lambda) \lambda^2 \exp(-2u_0 h) J_0(\lambda s) d\lambda, \quad (1)$$

where  $s$  is the coil separation,  $\lambda$  is the variable of integration, and  $J_0$  the Bessel function of the first kind of order zero. The term  $R(\lambda)$  can be written as

$$R(\lambda) = \frac{Y_1 - Y_0}{Y_1 + Y_0}, \quad (2)$$

where  $Y_0 = u_0 / i\omega\mu_0$  is the intrinsic admittance of free space,  $Y_1$  is the surface admittance,  $i$  is the imaginary number,  $\omega$  is the angular frequency,  $\mu_0$  is the magnetic permeability of free space, and  $u_0$  is equal to  $(\lambda^2 + k_0^2)^{1/2}$ , where  $k_0$  is the wave number of free space. For a  $L$ -layer earth,  $Y_1$  can be obtained by the following recurrence relation:

$$Y_\ell = \hat{Y}_\ell \frac{Y_{\ell+1} + \hat{Y}_\ell \tanh(u_\ell t_\ell)}{\hat{Y}_\ell + Y_{\ell+1} \tanh(u_\ell t_\ell)}, \quad \ell = 1, 2, \dots, L-1, \quad (3)$$

where

$$\hat{Y}_\ell = \frac{u_\ell}{i\omega\mu_0\mu_\ell} \quad (4)$$

and

$$u_\ell = (\lambda^2 + k_\ell^2)^{1/2}, \quad (5)$$

where  $k_\ell$  is the wave number of  $\ell$ -th layer given by

$$k_\ell = (i\omega\sigma_\ell\mu_0\mu_\ell - \omega^2\varepsilon_0\mu_0\mu_\ell)^{1/2}, \quad (6)$$

and where  $t_\ell$  is the thickness,  $\mu_\ell$  is the relative magnetic permeability,  $\sigma_\ell$  is the conductivity of the  $\ell$ th layer, and  $\varepsilon_0$  is the dielectric permittivity of free space. In practice, the reciprocal of the conductivity, the resistivity  $\rho_\ell$ , is commonly used. Here, for convenience, we note the  $\ell$ th layer relative permeability as  $\mu_\ell$  instead of  $\mu_{r\ell}$ . Further, since we employ the quasi-static assumption, equation (6) becomes

$$k_\ell = (i\omega\sigma_\ell\mu_0\mu_\ell)^{1/2}. \quad (7)$$

In the half-space at the bottom of the electrical section,

$$Y_L = \hat{Y}_L. \quad (8)$$

$Y_1$  is a complex function of an integral variable  $\lambda$ , the angular frequency  $\omega$ , the magnetic permeability  $\mu$ , the resistivity  $\rho$ , and the thickness  $t$  of the layers. For a given model,  $Y_1$  can be calculated by using the recurrence relationship in equations (3)–(5). Then,  $Y_1$  can be substituted into equations (2) and then into (1) to yield the responses of the system over the model.

Figure 2 presents the forward modeling results for horizontal coplanar coils over a homogeneous half-space (Huang and Fraser, 2000). The in-phase and quadrature components of the response function  $M + iN$  are shown as functions of the induction number  $\theta = (\omega\sigma\mu h^2)^{1/2}$  for various values of the relative

magnetic permeability  $\mu_r = \mu/\mu_0$ . The effect of a magnetic permeability  $\mu$  greater than the free space  $\mu_0$  is twofold. First, the permeability increases the value of the induction number  $\theta$ . Secondly, as  $\theta \rightarrow 0$ , the response function  $M + iN$  becomes dominated by the magnetization effect which is in-phase with, and in the same direction as, the primary field. This is the induced magnetization, which occurs for an alternating magnetic field of a coil just as it does for the static magnetic field of the earth. Thus, the in-phase component  $M$  of the response function becomes frequency independent, and the quadrature component  $N$  tends to zero as the induction number  $\theta$  approaches zero. At the other extreme, when the induction number is large, the induced conductive response completely overwhelms the magnetization effect. All curves in Figure 2 converge to that for  $\mu_r = 1$  as  $\theta \rightarrow \infty$ . For mid-range induction numbers, the magnetization and conductive effects are mixed. The in-phase component  $M$ , which becomes frequency dependent, could be either positive or negative depending upon the relative permeability and induction number.

### THE INVERSE PROBLEM

Traditional inversion techniques for solving nonlinear inverse problems were used in our study. An objective function was minimized subject to fitting the data in the least-squares sense. A brief outline will be given here. More details can be found in Lawson and Hanson (1974) and Menke (1984).

The data vector  $\mathbf{d}$  is defined as a set of measured data  $\mathbf{d} = [d_1, d_2, \dots, d_N]^T$  and the model parameter vector  $\mathbf{p}$  is a set of unknown model parameters  $\mathbf{p} = [p_1, p_2, \dots, p_M]^T$ , where  $T$  is the transpose,  $N$  is the number of measured data, and  $M$  is the number of model parameters. For helicopter EM measurements using Dighem systems, the set of measured data are

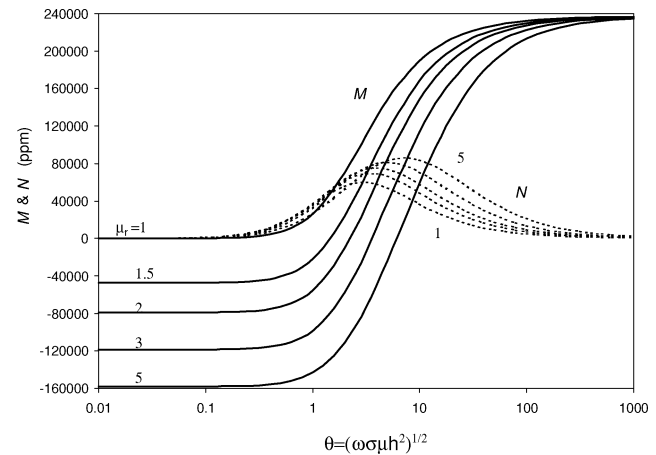


FIG. 2. In-phase  $M$  and quadrature  $N$  components of the response function of a homogeneous half-space versus the induction number  $\theta$  for various values of the relative magnetic permeability  $\mu_r$ .  $M$  and  $N$  are the measured in-phase  $I$  and quadrature  $Q$  components scaled for variations in flying height  $h$  and coil separation  $s$ , where  $I = M(s/h)^3$  and  $Q = N(s/h)^3$ . This relationship is valid on the assumption that  $s^3 \ll h^3$ , a condition that is normally met on all commercial frequency-domain helicopter EM surveys (Huang and Fraser, 2000). The in-phase  $I$  and quadrature  $Q$  components are in parts per million (ppm) of the primary field at the receiving coil, and so the rescaled  $M$  and  $N$  are also in ppm.

the in-phase and quadrature components at each frequency for the given altimeter. For a layered earth described here, the set of unknown model parameters are the resistivity, magnetic permeability, and thickness of each layer.

The functional relationship between the model parameters and the EM responses defined in equation (1) can be rewritten as

$$d_i = F_i(\mathbf{p}), \quad i = 1, 2, \dots, N. \quad (9)$$

For the helicopter EM problem, the function  $F_i(\mathbf{p})$  is highly nonlinear. To linearize the problem locally, we expand  $F_i(\mathbf{p})$  in a Taylor series around an initial model parameter vector  $\mathbf{p}^0$  for the first iteration and neglect the higher-order terms. Thus, we obtain  $\Delta\mathbf{p} = \mathbf{A}\Delta\mathbf{d}$ , where  $\Delta\mathbf{d}$  is a vector of differences between the measured data and the response of the initial model, and  $\Delta\mathbf{p}$  is an unknown vector to be solved, consisting of differences between the updated and initial model parameters  $\mathbf{p}$  and  $\mathbf{p}^0$ , respectively.  $\mathbf{A}$  is an  $N \times M$  matrix referred to as the Jacobian partial derivative or sensitivity matrix. Its elements are given by

$$a_{ij} = \frac{\partial F_i}{\partial p_j}, \quad i = 1, 2, \dots, N, \quad j = 1, \dots, M. \quad (10)$$

Using singular value decomposition (SVD), we have  $\mathbf{A} = \mathbf{U}\mathbf{\Lambda}\mathbf{V}^T$ , where  $\mathbf{U}$  is an  $N \times N$  data eigenvector matrix,  $\mathbf{V}$  is an  $M \times M$  parameter eigenvector, and  $\mathbf{\Lambda}$  is an  $N \times M$  diagonal matrix whose elements  $\lambda_j$  are the singular values. Then, the model parameter vector correction  $\Delta\mathbf{p}$  can be approximately calculated by

$$\Delta\mathbf{p} = \mathbf{V}\mathbf{\Lambda}^{-1}\mathbf{U}^T \Delta\mathbf{d}, \quad (11)$$

where elements in  $\mathbf{\Lambda}^{-1}$  are  $1/\lambda_j$ . A small singular value tends to yield a large contribution to  $\Delta\mathbf{p}$ . This may place a new solution outside the region where the Taylor series expansion is valid, and therefore make the inversion unstable. To stabilize the inverse procedure, we use Marquardt's method, and equation (11) can be modified as

$$\Delta\mathbf{p} = \mathbf{V}\mathbf{\Lambda}(\mathbf{\Lambda}^2 + e^2\mathbf{I})^{-1}\mathbf{U}^T \Delta\mathbf{d}, \quad (12)$$

where  $\mathbf{I}$  is the identity matrix and  $e^2$  is the damping parameter. The damping factor is defined as a percentage of the largest singular value  $\lambda_1$ . The percentage is larger in the beginning of the iteration procedure and gradually decreases as the model parameters are improved.

Then, an updated model parameter vector at the  $k$ th iteration is given by  $\mathbf{p}^k = \mathbf{p}^{k-1} + \Delta\mathbf{p}$ . The misfit  $\chi^2$ , given by

$$\chi^2 = \frac{1}{N} \sum_{i=1}^N \left[ \frac{d_i - F_i}{s_i} \right]^2, \quad (13)$$

will be minimized in the least-squares sense;  $s_i$  is the uncertainty in the  $i$ th datum, assuming data errors to be uncorrelated. In the case of nonlinear problems, several iterations are required before an acceptable solution is obtained in terms of minimizing the misfit between the measured data and the model responses.

#### CALCULATION OF THE JACOBIAN MATRIX

Inversion methods based on the linearization of nonlinear functions depend critically on the ability to estimate the

Jacobian matrix. The most generally applicable way of computing the partial derivatives is to use a finite-difference technique. However, it is only accurate to the second order for the central difference and to the first order for the forward difference. The disadvantage of finite-difference schemes is not only that they produce errors, but also that they are computationally intensive. Errors in the computation of the partial derivatives lead to instabilities during the inversion. To avoid these problems, an analytic method will be used here to compute the partial derivatives.

The partial derivatives in equation (10) can be computed analytically from equations (2) and (3), where the derivatives with respect to the model parameters involves only the term  $R(\lambda)$  in equation (1). Thus, we can write

$$\frac{\partial R}{\partial p_\ell} = \frac{\partial R}{\partial Y_1} \frac{\partial Y_1}{\partial p_\ell} = \frac{2Y_0}{(Y_1 + Y_0)^2} \frac{\partial Y_1}{\partial p_\ell}, \quad (14)$$

where  $p_\ell$  represents a model parameter in  $\ell$ th layer, which can be resistivity, permeability or thickness.

From equation (3), we can write

$$\frac{\partial Y_1}{\partial p_\ell} = \frac{\partial Y_1}{\partial Y_2} \frac{\partial Y_2}{\partial Y_3} \dots \frac{\partial Y_{\ell-1}}{\partial Y_\ell} \frac{\partial Y_\ell}{\partial p_\ell}. \quad (15)$$

Differentiating equation (3), we have

$$\frac{\partial Y_\ell}{\partial Y_{\ell+1}} = \frac{(\hat{Y}_\ell)^2 [1 - \tanh^2(u_\ell t_\ell)]}{[\hat{Y}_\ell + Y_{\ell+1} \tanh(u_\ell t_\ell)]^2}, \quad (16)$$

The derivatives of  $Y_\ell$  with respect to each model parameter  $p_\ell$  in the  $\ell$ th layer can be easily obtained from equation (3). Finally, the partial derivatives of the response with respect to the earth parameters can be obtained by replacing  $R(\lambda)$  by equation (14) in equation (1).

We may use partial derivatives to show the impact of magnetic permeability on the EM response. Figure 3 presents the partial derivatives of the in-phase and quadrature components of the response function, with respect to the magnetic permeability of a homogeneous half-space, as a function of the induction number  $\theta$ . Whereas magnetic permeability can have a huge effect on the in-phase partial derivative, we also see that the effect on the quadrature component can be significant.

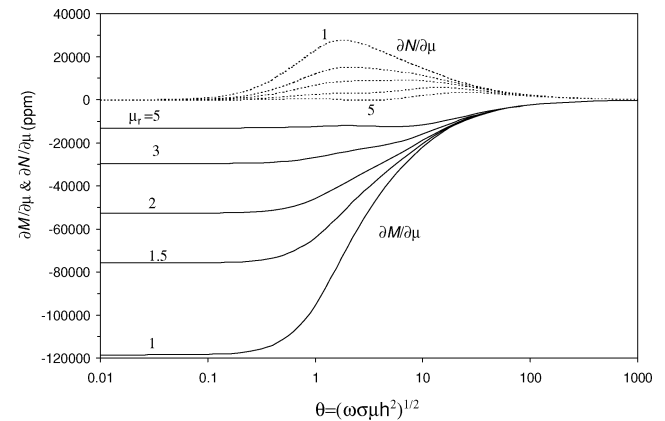


FIG. 3. Partial derivatives of the in-phase and quadrature components of the response function for a homogeneous half-space versus the induction number  $\theta$  for various values of the relative magnetic permeability  $\mu_r$ .

Large absolute values of the partial derivatives of Figure 3 indicate good resolvability in parameter determination, whereas values close to zero indicate poor reliability. When the induction number  $\theta \ll 1$ , the partial derivatives of the in-phase are frequency independent, whereas those of the quadrature are almost zero. A small variation in magnetic permeability causes a large change in the partial derivative of the in-phase component, indicating that the magnetic permeability can be well determined from the in-phase data at low induction number. The absolute value of the in-phase derivative decreases as the magnetic permeability increases. This means that the resolvability may be better for materials of low magnetic permeability than for highly magnetic materials. For the mid-range values of the induction number  $\theta$ , the derivatives of the in-phase component become frequency dependent, and their absolute values decrease. Those of the quadrature component increase as  $\theta$  increases, until they reach local maxima, and then they decrease. The resolvability of the magnetic permeability decreases at the higher induction numbers, but the use of both the in-phase and quadrature data aids in the resolution of the magnetic permeability. As  $\theta \rightarrow \infty$ , the derivatives for different magnetic permeabilities tend to be identical and approach zero, whereupon permeability determinations become impossible.

#### INVERSION OF SYNTHETIC DATA

##### Detection of magnetic basement

The inversion technique is demonstrated on synthetic, noise-free data using three typical Dighem frequencies of 56000,

7200, and 900 Hz, each with a transmitting-receiving coil separation of 8 m. Our first example employs a two-layer model (insert to Figure 4a) to simulate the common situation of moderately conductive, nonmagnetic overburden overlying a moderately resistive and magnetically permeable basement. The upper layer has a resistivity  $\rho_1$  of 50 ohm-m, a relative magnetic permeability  $\mu_1$  of 1 (free space) and a thickness  $t_1$  of 15 m. The basement has a resistivity  $\rho_2$  of 500 ohm-m and a relative magnetic permeability  $\mu_2$  of 1.05. The goal is to resolve model parameters  $\rho_1$ ,  $\rho_2$ ,  $\mu_2$ , and  $t_1$  given our knowledge that the overburden is nonmagnetic and so  $\mu_1$  is fixed at the free space value.

The inversion results for the model are shown in Figure 4. Figures 4a, 4b, and 4c respectively illustrate how the model parameters of resistivity, thickness, and permeability change after each iteration. The starting model (iteration = 0) is determined directly from the resistivity-depth transform of Huang and Fraser (1996) and the apparent permeability transform of Huang and Fraser (2000). The upper-layer resistivity  $\rho_1$  and basement permeability  $\mu_2$  reach their correct values after three and four iterations, respectively. The basement resistivity  $\rho_2$  converges more slowly, yielding the correct value at the 6th iteration. Figure 4d presents the decrease in the misfit  $\chi^2$  as defined in equation (13), which is normalized by the misfit at the 0th iteration. The misfit is reduced by more than five orders of magnitude in six iterations.

We now examine the same model but with a varying depth to basement. Figure 5a presents a two-layer model where the thickness  $t_1$  of the upper layer is variable. Its resistivity and

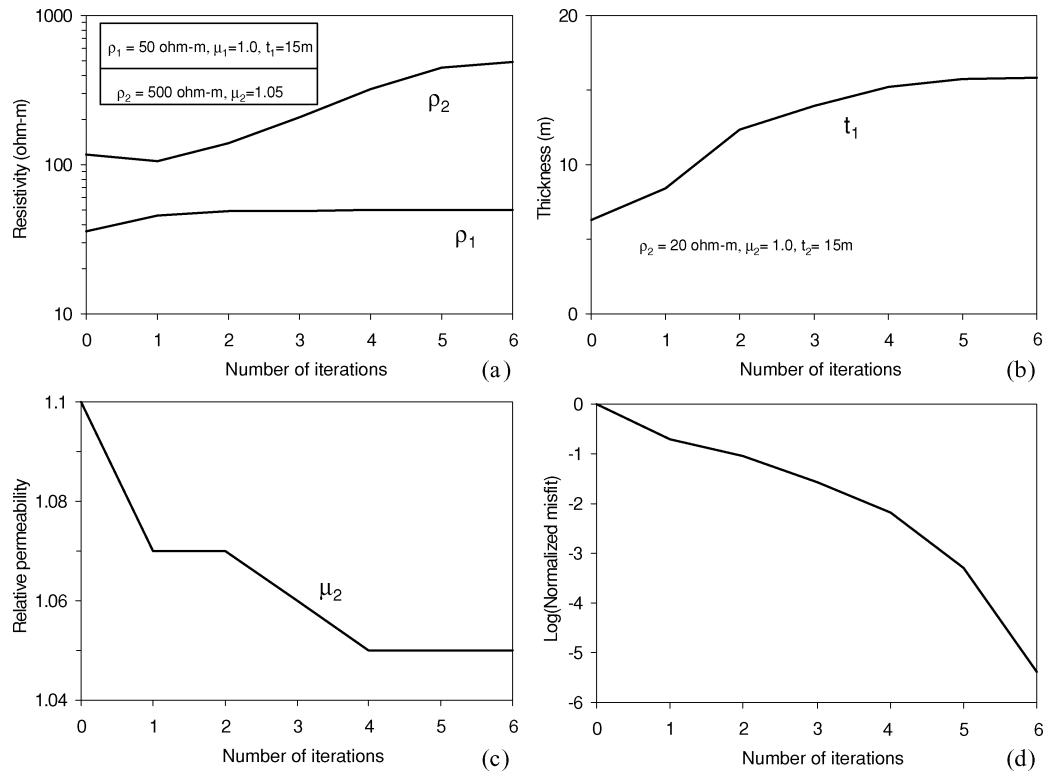


FIG. 4. The results of an inversion for a two-layer model, where  $\rho_1 = 50$  ohm-m,  $\rho_2 = 500$  ohm-m,  $\mu_1 = 1$ ,  $\mu_2 = 1.05$  and  $t_1 = 15$  m. The model parameters for (a)  $\rho_1$  and  $\rho_2$ , (b)  $t_1$ , (c)  $\mu_2$ , and (d) the associated misfit are shown as a function of the number of iterations. The input data comprised the in-phase and quadrature components computed at frequencies of 56000, 7200, and 900 Hz for a sensor height of 30 m.

permeability are the same as that in Figure 4, but the depth to basement increases at each data station in steps from 1 m on the left to 100 m on the right. The EM responses were computed from 1D models at each data station and then used in the inversion. The computed resistivity-depth and susceptibility-depth sections obtained from the 1D inversions are presented respectively in Figures 5b and 5c. In Figure 5c, we transformed the relative magnetic permeability into the susceptibility  $\kappa = \mu_r - 1$  in SI units to increase the sensitivity for display purposes. The starting model at the leftmost station is determined from the resistivity-depth and permeability algorithms as described above. Then, the inversion results for this station serve as the starting model for next station, and so on for each of the following stations.

In Figure 5, both the resistivity and the susceptibility of the basement are well resolved for mid-range thicknesses of the upper layer. However, when the thickness is too small, as on the left side of the section, the model parameters  $\rho_2$  and  $\mu_2$  for the basement are overestimated, although the image has reasonably recovered the model. On the right side of the section, where the overburden is thick, the basement resistivity is underestimated while its susceptibility is slightly overestimated. For the upper layer, the resistivity and thickness are well resolved apart from the left side of Figure 5, where the

thickness varies from 1 to 1.8 m. In this range of true thicknesses, the computed upper layer resistivity ranges from 73 to 51 ohm-m while the calculated thickness ranges from 1.60 to 1.85 m.

The resolvability of the model parameters may be evaluated from the partial derivatives. Figure 6 shows the absolute value of the partial derivatives of the in-phase  $I$  and quadrature  $Q$  components with respect to the model parameters as functions of frequency and depth to basement  $t_1$  for the model of Figure 5a. It can be seen that the resolvability for each individual parameter varies with the depth to basement and the frequency. The upper-layer resistivity  $\rho_1$  (see Figures 6a, b) can be determined from the high-frequency data at a depth to basement from a few meters up to 100 m, with the best resolvable zone occurring at a depth of about 10 m. The behavior of the derivatives with respect to  $\rho_2$  (Figures 6c, d) is similar to that for  $\rho_1$ , but it is the least resolvable parameter since the partial derivatives are close to zero, and its solution becomes difficult when the thickness  $t_1$  of the upper layer is greater than about 30 m. The upper-layer thickness  $t_1$  (Figures 6e, f) will be mainly determined from the data at the higher frequencies. The permeability of the basement (Figures 6g, h) may be determined from the in-phase data at the lower frequencies and the quadrature data at the higher frequencies. The ability

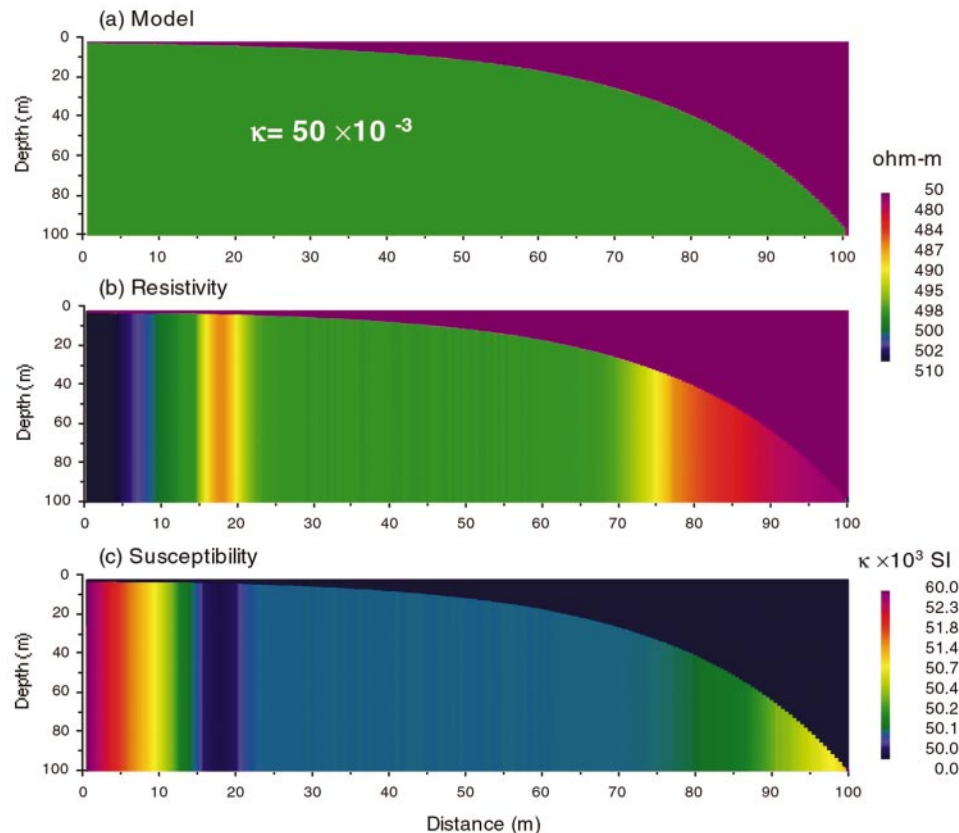


FIG. 5. (a) A continuous series of 1D two-layer earth models where the thickness of the upper layer  $t_1$  increases in small but discrete steps from left to right, and the interface between the two is shown as a color contrast that coincides with these steps. The model parameters are the same as those in Figure 4 except that  $t_1$  varies from 1 m on the left to 100 m on the right. The model of (a) was used to generate the in-phase and quadrature components at the three frequencies. These data were inverted to provide (b) the imaged resistivity-depth section stitched from the results of the 1D inversions, and (c) the imaged magnetic susceptibility-depth section.

to resolve the permeability of the basement is reduced as the overburden becomes deeper, as expected.

The narrow low-amplitude features in Figure 6 show that the derivatives cross zero. Zero derivatives indicate that the EM data are insensitive to changes in the model parameter. For example, the quadrature data in Figure 2 have amplitude peaks at the middle values of the induction number  $\theta$ . The derivative of the quadrature data with respect to conductivity  $\sigma$  will be zero at these peaks. Therefore, the quadrature data at the peak amplitudes would be not useful in resolving the conductivity.

### Detection of magnetic middle layer

We will use a three-layer model (insert to Figure 7a) to simulate the situation of a magnetic layer sandwiched between

nonmagnetic layers. The nonmagnetic upper layer of Figure 7a has a resistivity  $\rho_1$  of 200 ohm-m and a thickness  $t_1$  of 15 m. The variable-thickness middle layer has a resistivity  $\rho_2$  of 500 ohm-m and a permeability  $\mu_2$  of 1.05. The nonmagnetic basement has a resistivity  $\rho_3$  of 50 ohm-m. The model parameters to be resolved are  $\rho_1$ ,  $\rho_2$ ,  $\rho_3$ ,  $\mu_2$ ,  $t_1$ , and  $t_2$  using three-frequency data under the assumption that the upper and lower layers are non-magnetic. First, we examine how the iterations converge for a single model with  $t_2 = 30$  m, as shown in Figure 7a. The values for resistivity and thickness almost reach the true values after five and four iterations, respectively. The permeability needs six iterations to approach the correct value because the starting value is far from the true value. The normalized misfit  $\chi^2$  is reduced by more than five orders of magnitude in six iterations as seen in Figure 7d.

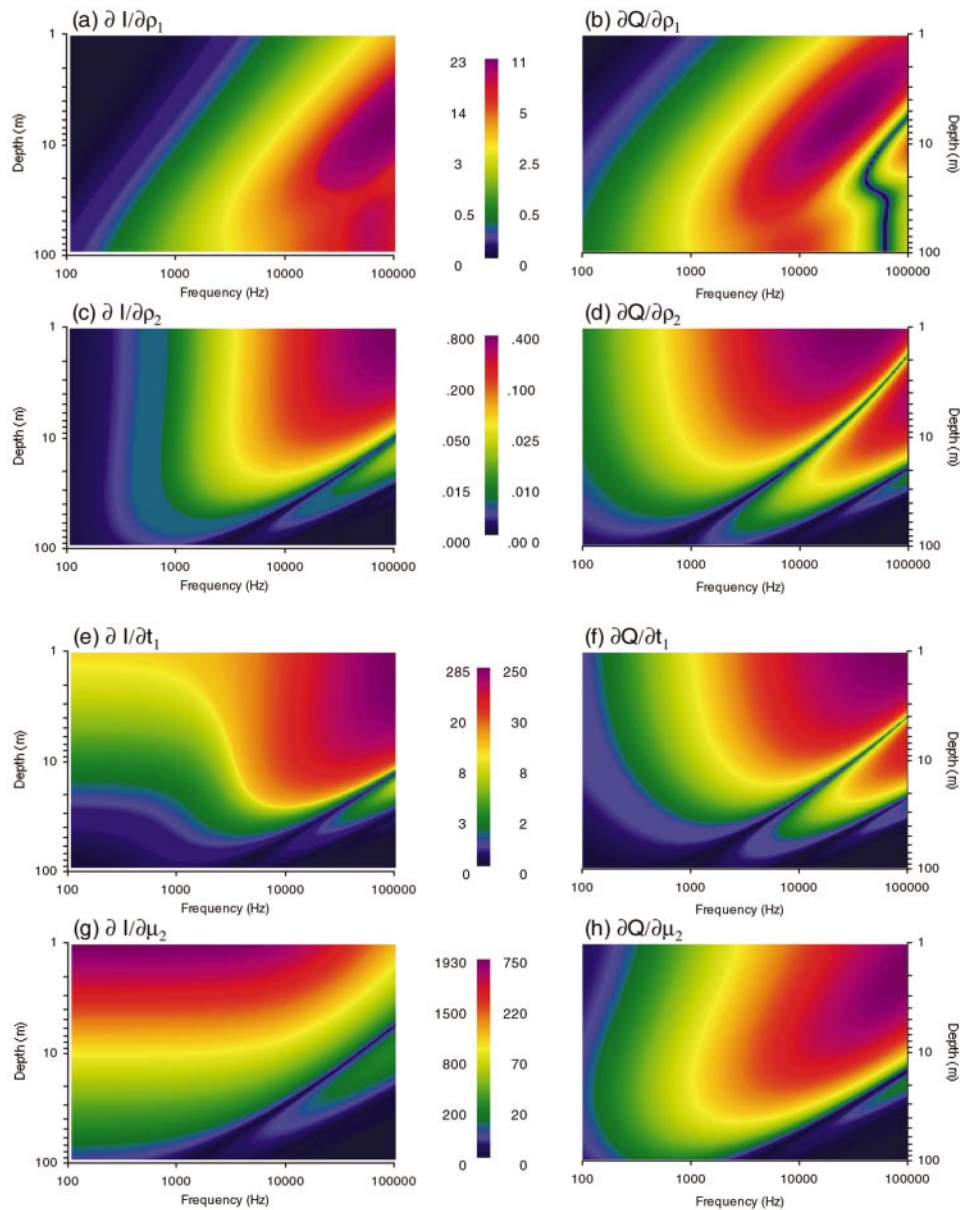


FIG. 6. Absolute magnitude of the partial derivatives of the in-phase  $I$  and quadrature  $Q$  components with respect to model parameters of (a, b)  $\rho_1$ , (c, d)  $\rho_2$ , (e, f)  $t_1$ , and (g, h)  $\mu_2$  for the 2D model in Figure 5. Values close to zero indicate poor reliability in parameter determination.

Figure 8 shows the inversion results for the model of Figure 8a using a 1-D approximation at each data station, in accordance with the description for Figure 5. The model of Figure 8a is the same as for Figure 7a but the thickness of the magnetically permeable middle layer ranges from 20 m on the left to 100 m on the right. The relative magnetic permeability was transformed into the susceptibility  $\kappa$  as described for Figure 5. The upper-layer resistivity and the thicknesses of the upper and middle layers are well resolved across the entire section. The correct value for the basement resistivity is obtained when the overlying magnetic layer is thin but, as its thickness increases, the inverted basement resistivity becomes somewhat higher than its true value of 50 ohm-m (although this may be difficult to discern from the color scheme of Figure 8b). The greatest variation from the true values occurs for the computed resistivity and susceptibility of the middle layer. The color legend shows that the resistivity of the middle layer tends to be underestimated for small thicknesses and overestimated for large thicknesses, and that the susceptibility is underestimated for large thicknesses.

### Multiple magnetic layers

We now examine models where two layers are magnetic. Figure 9 shows the inversion results for a two-layer model, where the true model is shown as an insert to Figure 9a. Five model parameters  $\rho_1$ ,  $\rho_2$ ,  $\mu_1$ ,  $\mu_2$ , and  $t_1$  are to be determined using the three-frequency data of 56000 Hz, 7200 Hz, and 900 Hz. Figures 9a, 9b, and 9c, respectively, illustrate how the model parameters of resistivity, thickness, and permeability change after

each iteration. As can be seen, the starting values for the resistivity and permeability are reasonably close to the true values. After six iterations, all parameters converge to the correct values, and the misfit  $\chi^2$  has been reduced by more than six orders of magnitude as shown in Figure 9d.

If the starting model is well selected, the iteration can approach the true model even for underdetermined problems, as shown in the example of Figure 10. This is a three-layer model with a nonmagnetic conductive layer sandwiched between magnetically permeable and moderately resistive layers, as shown in the insert to Figure 10b. There are eight model parameters to be inverted for six input EM data. All of the parameters have been estimated to within 2.5% of their true values after nine iterations. In Figure 10c, the magnetic permeability is displayed as susceptibility for reasons given above.

### FIELD EXAMPLE

We have inverted the in-phase and quadrature data at frequencies of 56000, 7200, and 900 Hz acquired from a Dighem survey over the copper-gold porphyry deposit at Mt. Milligan. This deposit is located in central British Columbia, Canada, and its geology is described briefly in Shives et al. (2000). We show the data for the same 13 data points used by Zhang and Oldenburg (1997) to allow a comparison between two different inversion techniques. Zhang and Oldenburg obtained their resistivity distribution by inverting 2D dc ground resistivity measurements. They used these inverted resistivities along with the helicopter EM data as input to their magnetic permeability inversion algorithm.

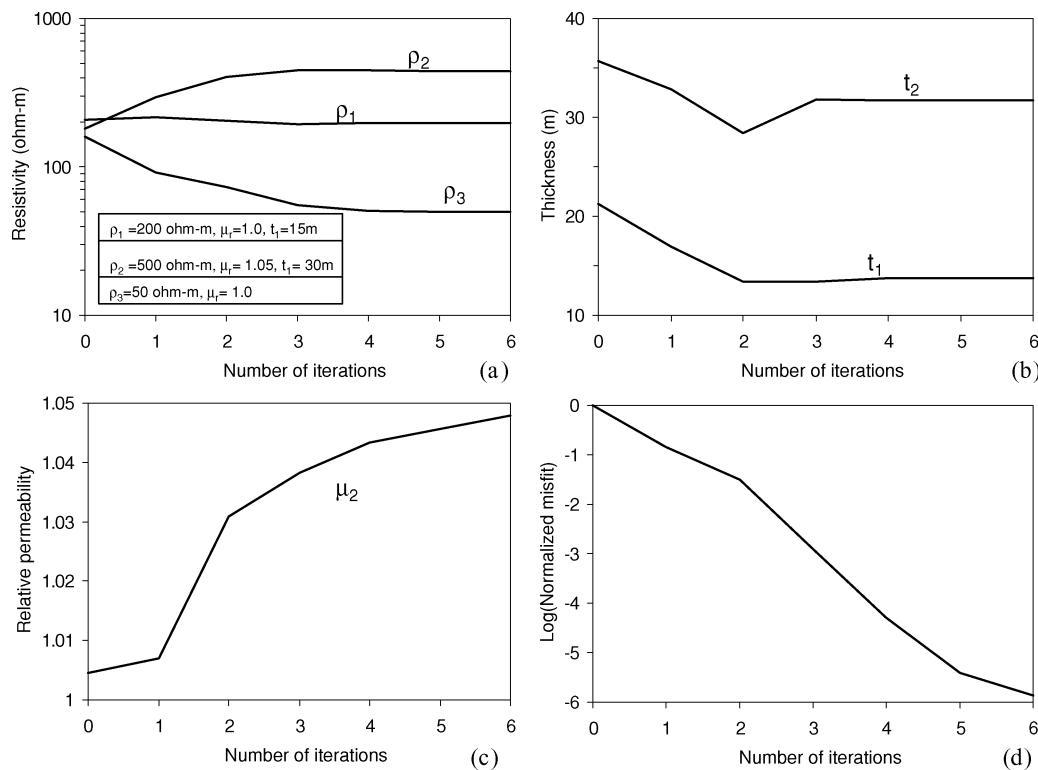


FIG. 7. The results of an inversion for a three-layer model, where  $\rho_1 = 200$  ohm-m,  $\rho_2 = 500$  ohm-m,  $\rho_3 = 50$  ohm-m,  $\mu_1 = 1$ ,  $\mu_2 = 1.05$ ,  $\mu_1 = 1$ ,  $t_1 = 15$  m, and  $t_2 = 30$  m. The model parameters for (a)  $\rho_1$ ,  $\rho_2$ , and  $\rho_3$ , (b)  $t_1$  and  $t_2$ , (c)  $\mu_2$ , and (d) the associated misfit are shown as a function of the number of iterations.

Figures 11a and 11b respectively show the Dighem sensor height and the three-frequency EM data for the 13 data points, and Figure 11c shows the apparent susceptibility obtained from the transform technique developed by Huang and Fraser (2000). As discussed above, a magnetic permeability that is greater than free space may cause the in-phase data at the lower frequencies to become negative. Figure 11b shows that the in-phase data at 900 Hz are negative across the center part of the profile, with the maximum negative value occurring at station 12.9 km. This station corresponds to the computed apparent susceptibility high in Figure 11c.

The inversion was performed using a three-layer model. Eight parameters  $\rho_1$ ,  $\rho_2$ ,  $\rho_3$ ,  $\mu_1$ ,  $\mu_2$ ,  $\mu_3$ ,  $t_1$ , and  $t_2$  were inverted using the six in-phase and quadrature data of Figure 11b and the sensor height of Figure 11a. Figures 12a and 12b respectively show the inverted and imaged resistivity and susceptibility. The inversion results from Zhang and Oldenburg (1997) are shown in Figure 13 for comparison.

The conductivity model in Figure 13a was obtained by Zhang and Oldenburg (1997) from their inversion of 2D dc ground resistivity data using 22 layers. This conductivity model was used as an input, along with the helicopter EM data, to invert for the susceptibility. Their susceptibility inversion was performed using the same 22 layers as used in their inversion of the dc ground resistivity data. The magnetite concentration,

visually estimated from borehole samples over the same section, is shown in Figure 13c, and the susceptibility obtained from the 3D inversion of static ground magnetic data is shown in Figure 13d. The authors have explained the discrepancies between Figures 13b, c, and d. Our discussion will be focused on a comparison of our inversion results of Figure 12 with their inversion results of Figures 13a and 13b.

A comparison of the resistivity section in Figure 12a to the conductivity ( $= 1/\text{resistivity}$ ) section in Figure 13a shows that similar conductive features appear at both ends of the profile on both sections. However, the conductivity section of Figure 13a has a different appearance because the inversion is based on a 22-layer model with a smoothly varying presentation across the layers versus the discrete three-layer presentation of Figure 12a, and also because different data sets were used.

There are three susceptibility highs in Figure 13b. The largest has an amplitude of 0.1 SI and occurs at station 12.9 km at a depth of about 20 m. This body has a thickness of 100 m or more. The susceptibility section from the three-layer inversion of Figure 12b has a magnetic middle layer with the strongest susceptibility occurring at this same station, but the amplitude of 0.247 SI is much larger than in Figure 13b. The thickness of the magnetic layer at this station is about 70 m in Figure 12b, which is thinner than that from the 22-layer inversion of Figure 13b and from the ground magnetic inversion of Figure 13d.

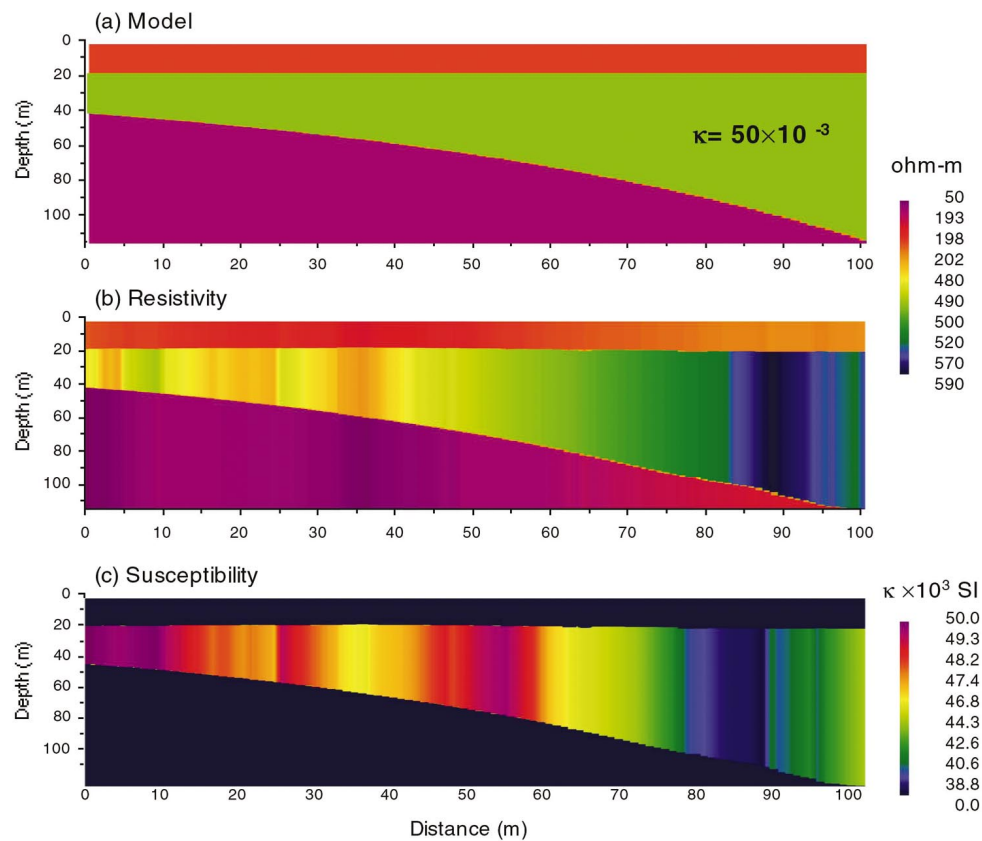


FIG. 8. (a) Two-dimensional model simulated by a number of 1D models, (b) the imaged resistivity-depth section stitched from the results of the 1D inversions, and (c) the magnetic susceptibility-depth section. The model parameters are the same as those in Figure 7 except for  $t_2$ , which ranges from 20 m on the left to 100 m on the right.

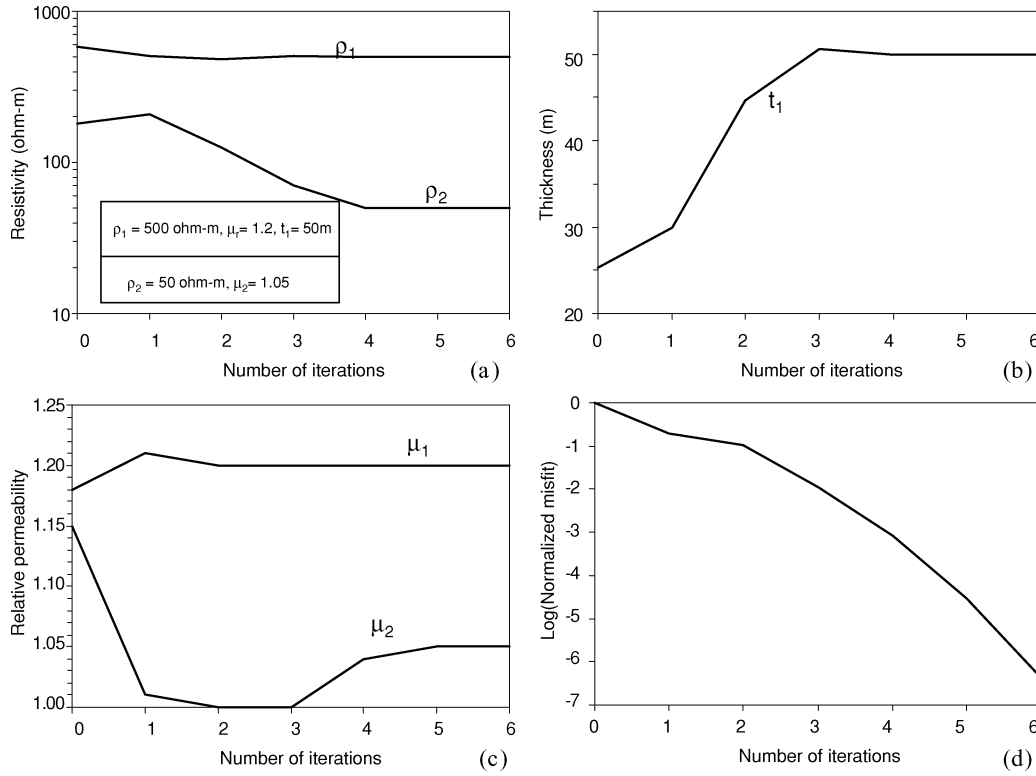


FIG. 9. The results of an inversion for a two-layer model, where  $\rho_1 = 500$  ohm-m,  $\rho_2 = 50$  ohm-m,  $\mu_1 = 1.2$ ,  $\mu_2 = 1.05$  and  $t_1 = 50$  m. The model parameters for (a)  $\rho_1$  and  $\rho_2$ , (b)  $t_1$ , (c)  $\mu_1$  and  $\mu_2$ , and (d) the associated misfit are shown as a function of the number of iterations.

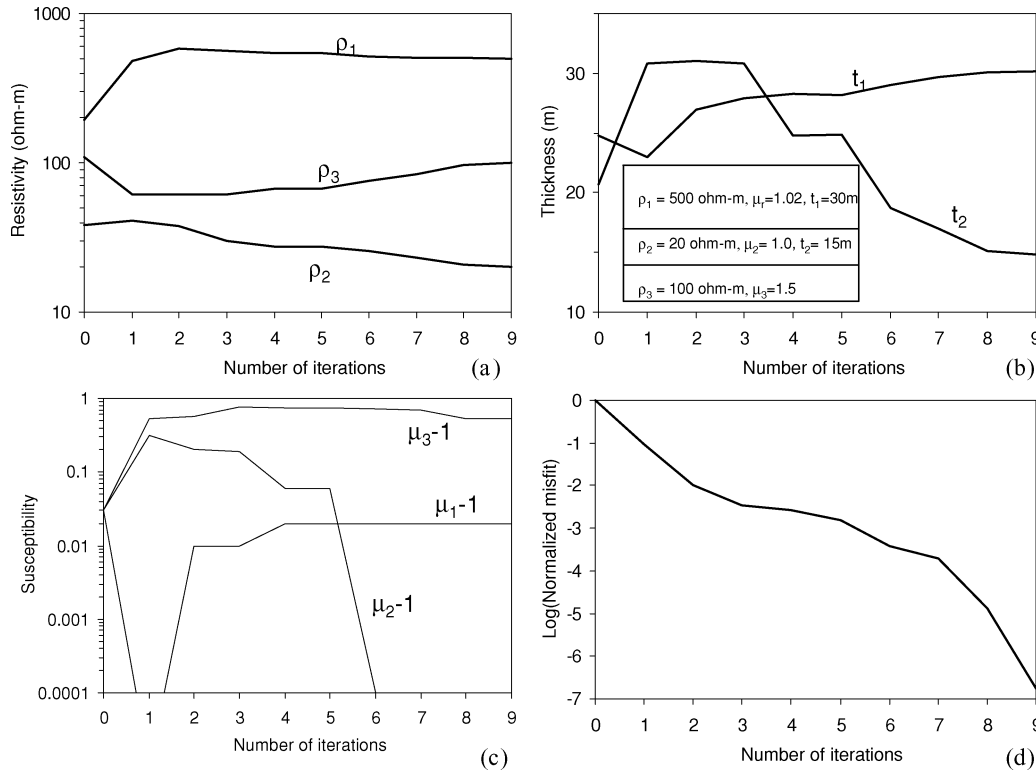


FIG. 10. The results of an inversion for a three-layer model, where  $\rho_1 = 500$  ohm-m,  $\rho_2 = 20$  ohm-m,  $\rho_3 = 100$  ohm-m,  $\mu_1 = 1.02$ ,  $\mu_2 = 1.0$ ,  $\mu_3 = 1.5$ ,  $t_1 = 30$  m, and  $t_2 = 15$  m. The model parameters for (a)  $\rho_1$ ,  $\rho_2$ , and  $\rho_3$ , (b)  $t_1$  and  $t_2$ , (c)  $\mu_1$ ,  $\mu_2$ , and  $\mu_3$ , and (d) the associated misfit are shown as a function of the number of iterations. The magnetic permeability parameter is plotted as susceptibility to show the smaller values more clearly.

The second strongest susceptibility high occurs at station 13.1 km in Figure 13b and at 13.2 km in Figure 13d. It is located at 13.1–13.2 km according to our inversion of Figure 12b. The 0.2-SI susceptibility from our inversion of Figure 12b is larger than the 0.06 SI of Figure 13b.

The third susceptibility feature in Figure 13b occurs at stations 12.5–12.7 km, and this location correlates with our inversion in Figure 12b. Again, the 0.05–0.18-SI susceptibility from our inversion in Figure 12b is larger than the 0.005–0.015 SI of Figure 13b.

There is a disagreement between the two inversions with respect to the amplitude of the magnetic susceptibility. Values

obtained from our inversion are 2–10 times higher than those obtained from the 22-layer inversion of Zhang and Oldenburg (1997). The discrepancy may be caused in part by the different resistivity sections. Resistivities range from 120 to 2000 ohm-m in Figure 13a (derived from their ground dc data) versus 80 to 1500 ohm-m in our section of Figure 12a (from the helicopter EM data). In our case, inverting for the resistivity and the susceptibility simultaneously using the same data set may improve the quality of the inversion. On the other hand, our use of a single data set may increase the likelihood of nonuniqueness in the inversion, resulting in a poorer solution.

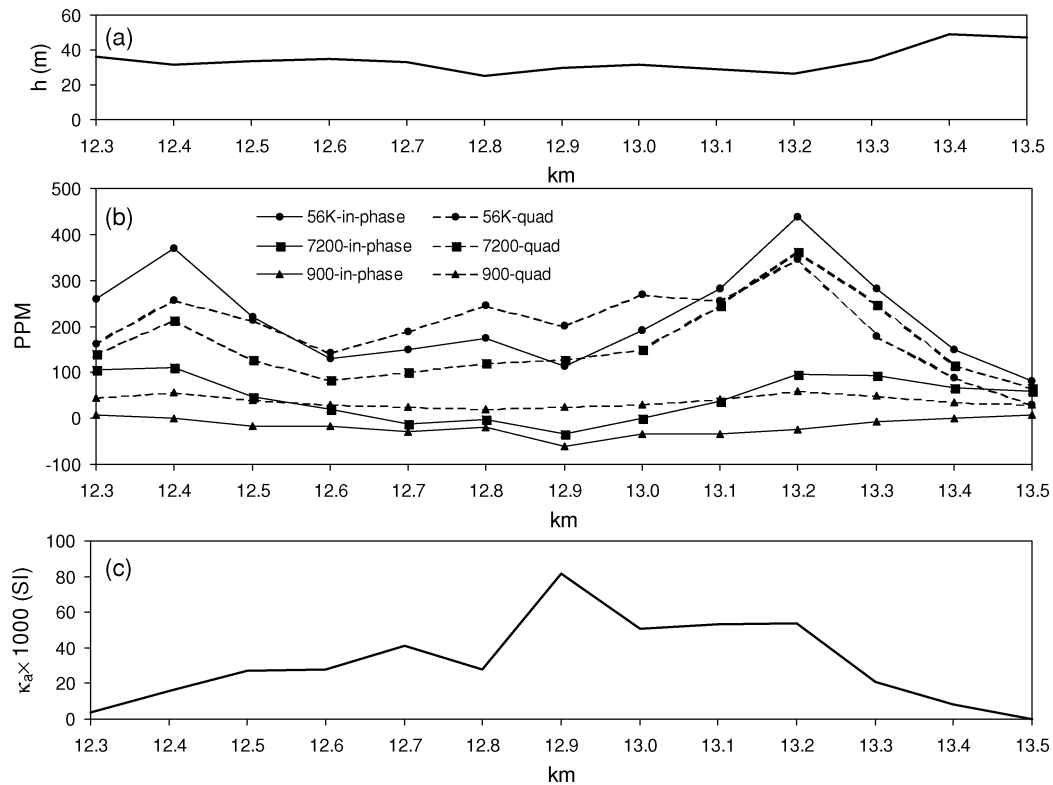


FIG. 11. Dighem data from Mt. Milligan. (a) The EM sensor height, (b) the three-frequency EM data, and (c) the computed apparent susceptibility.

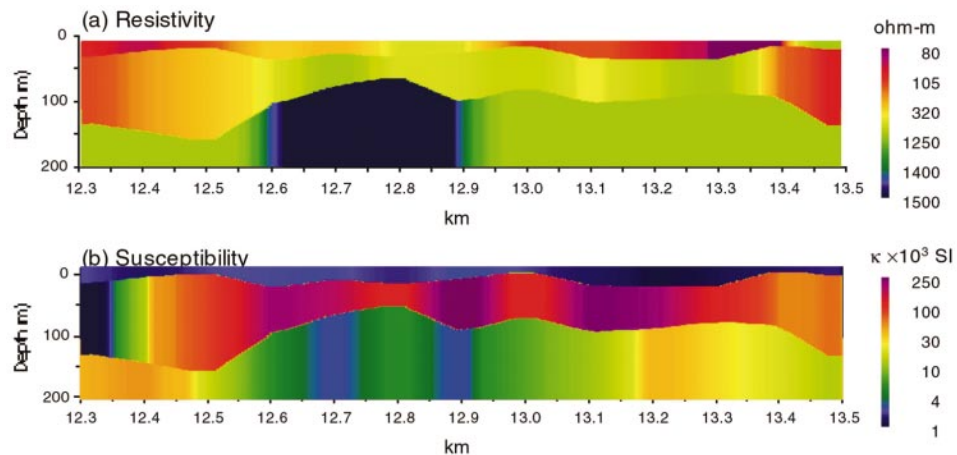


FIG. 12. (a) Resistivity and (b) susceptibility sections from inversion of the Dighem data of Figures 11a and 11b using a three-layer model.

An examination of the borehole data of Figure 13c may be illuminating. We may convert the computed susceptibilities (of Figures 12b and 13b) to percent magnetite using the empirical formula,  $\kappa_c = 2.89 \times 10^{-3} V^{1.01}$ , where  $\kappa_c$  is the magnetic susceptibility in cgs units and  $V$  is the volume-percent magnetite (Mooney and Bleifuss, 1953). The percent magnetite obtained using this formula at three locations is shown in Table 1 for our three-layer inversion and for the 22-layer inversion of

**Table 1. Percent magnetite at three locations in Figures 12 and 13 calculated from the inverted susceptibilities using the empirical formula of Mooney and Bleifuss (1953).**

Location along the section	12.7 km	12.9 km	13.1 km
Visual estimate from boreholes	3.5–4.5	5–8	3.5–4.5
From three-layer inversion	4.2	6.7	5.4
From 22-layer inversion	1.1	2.7	1.6

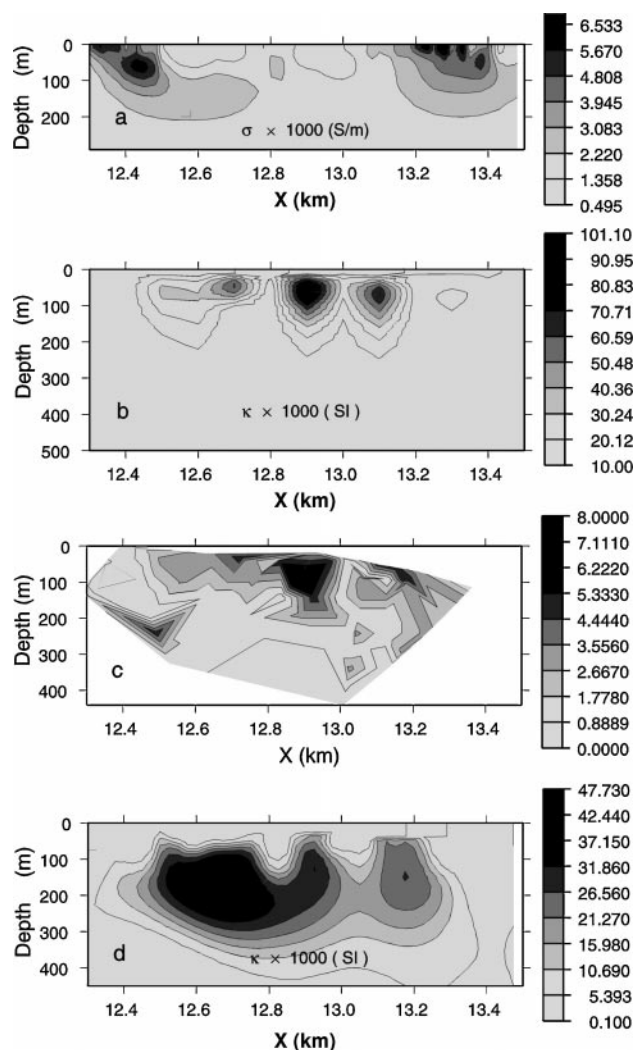


FIG. 13. Inversion of data from Mt. Milligan by Zhang and Oldenburg (1997). (a) Conductivity from the inversion of 2D dc ground resistivity data. (b) Magnetic susceptibility from the 1D inversion of Dighem EM data using the conductivity from (a) as an input. (c) Volume percent magnetite from borehole information. (d) Susceptibility from the 3D inversion of static ground magnetic data.

Zhang and Oldenburg (1997). The magnetite percentages obtained from our three-layer inversion are closer to the borehole estimates.

Regardless of the differences between the two inversions, they both identify susceptibility highs at stations 12.6–12.7 km, 12.9 km, and 13.1–13.2 km, and these highs occur at nearly the same depths and with similar depth extents. Therefore, we conclude that our results compare generally to those obtained by Zhang and Oldenburg (1997) from their ground geophysical data, notwithstanding the paucity of our three-frequency airborne data.

Part of the motivation for our research was to provide an analytic tool that would be expected to have application for a future digital sensor (Dighem<sub>Res</sub><sup>V</sup>) having five horizontal coplanar transmitting-receiving coil-pairs with frequencies geometrically spaced in the interval from 380 to 100000 Hz. Such a sensor would yield ten in-phase plus quadrature data points per sample, rendering improved inversion results.

## CONCLUSIONS

An algorithm has been developed for calculating the resistivity, magnetic permeability, and thickness of a layered earth from the inversion of multifrequency helicopter EM data. The technique follows traditional inversion methodologies for solving nonlinear inverse problems by minimizing an objective function subject to fitting the data. Inversion of synthetic data indicates that the correct model parameters may be obtained after several iterations for two- and three-layer models using six in-phase and quadrature data from three frequencies.

It is well known that the inversion results can vary with the starting model. The starting model in this study was obtained from previously published half-space algorithms. However, once the inversion process is underway, a model obtained at the previous data point may serve as the starting model for the current station if the fit were acceptable, thereby reducing computing time.

The analysis of partial derivatives contributes to a better understanding of the relative importance of model parameters and the reliability of their determination. For a two-layer model with a magnetic resistive basement and a conductive nonmagnetic upper layer, for example, the basement permeability can be well determined in most situations while the basement resistivity remains the least reliable parameter. The data contribute differently to the determination of the model parameters. The in-phase data at the lower frequencies are more important in determining the susceptibility, whereas the determination of depth to basement can depend more on the higher frequency data.

The inversion method was tested on data from the Dighem helicopter EM system flown over Mt. Milligan, British Columbia, Canada. The inversion results compare generally with the results presented by Zhang and Oldenburg (1997).

## ACKNOWLEDGMENTS

Appreciation is expressed to Richard Smith and Peter Wolfgram for their helpful suggestions, and to Fugro Airborne Surveys for permission to publish this paper. Figure 13 was generated from a digital file kindly provided by D. W. Oldenburg.

## REFERENCES

- Beard, L. P., and Nyquist, J. E., 1998, Simultaneous inversion of airborne electromagnetic data for resistivity and magnetic permeability: *Geophysics*, **63**, 1556–1564.
- Fitterman, D. V., and Deszczpan, M., 1998, Helicopter EM mapping of saltwater intrusion in Everglades National Park, Florida: *Explor. Geophys.*, **29**, 240–243.
- Fraser, D. C., 1973, Magnetite ore tonnage estimates from an aerial electromagnetic survey: *Geoexploration*, **11**, 97–105.
- 1978, Resistivity mapping with an airborne multicoil electromagnetic system: *Geophysics*, **43**, 144–172.
- 1981, Magnetite mapping with a multicoil airborne electromagnetic system: *Geophysics*, **46**, 1579–1593.
- Fraser, D. C., Stodt, J. A., and Ward, S. H., 1990, The effect of displacement currents on the response of a high-frequency helicopter electromagnetic system, in Ward, S. H., Ed., *Geotechnical and environmental geophysics: II, Environmental and groundwater*: Soc. Expl. Geophys., 89–96.
- Frischknecht, F. C., 1967, Fields about an oscillating magnetic dipole over a two-layer earth and application to ground and airborne electromagnetic surveys: *Quarterly of the Colorado School of Mines*, **62**, No. 1.
- Holladay, S. J., Valleau, N., and Morrison, E., 1986, Application of multifrequency helicopter electromagnetic survey to mapping of sea-ice thickness and shallow-water bathymetry, in Palacky, G. J., Ed., *Airborne resistivity mapping*: Geol. Surv. Canada Paper 86-22, 91–98.
- Huang, H., and Fraser, D. C., 1996, The differential parameter method for multifrequency airborne resistivity mapping: *Geophysics*, **61**, 100–109.
- 2000, Airborne resistivity and susceptibility mapping in magnetically polarizable areas: *Geophysics*, **65**, 502–511.
- 2001, Mapping of the resistivity, susceptibility, and permittivity of the earth using a helicopter-borne electromagnetic system: *Geophysics*, **66**, 148–157.
- 2002, Dielectric permittivity and resistivity mapping using high-frequency helicopter-borne EM data: *Geophysics*, **67**, 727–738.
- Huang, H., and Palacky, G. J., 1991, Damped least-squares inversion of time-domain airborne EM data based on singular value decomposition: *Geophys. Prosp.*, **39**, 827–844.
- Huang, H., and Zhu, R., 1984, Interpretation method of the time-domain airborne electromagnetic response above a magnetic conductive sphere model, *J. Changchun College of Geology*, **1**, 107–116.
- Lawson, C. L., and Hanson, R. J., 1974, *Solving least-squares problems*: Prentice Hall, Inc.
- Lodha, G. S., and West, G. F., 1976, Practical airborne EM (AEM) interpretation using a sphere model: *Geophysics*, **41**, 1157–1169.
- Menke, W., 1984, *Geophysical data analysis—Discrete inverse theory*: Academic Press, Inc.
- Mooney, H. M., and Bleifuss, R., 1953, Magnetic susceptibility measurements in Minnesota, Part II, Analysis of field results: *Geophysics*, **18**, 383–393.
- Paterson, N. R., and Reford, S. W., 1986, Inversion of airborne electromagnetic data for overburden mapping and groundwater exploration, in Palacky, G. J., Ed., *Airborne resistivity mapping*: Geol. Surv. Canada Paper 86-22, 39–48.
- Qian, W., Gamey, J. T., Holladay, S. J., Lewis, R., and Abernathy, D., 1997, Inversion of airborne electromagnetic data using an Occam technique to resolve a variable number of layers, in *Proceedings of high-resolution geophysics workshop, SAGEEP*, **97**, 735–744.
- Sengpiel, K. P., and Siemon, B., 2000, Advanced inversion methods for airborne electromagnetic exploration, *Geophysics*, **65**, 1983–1992.
- Shives, R. B. K., Charbonneau, B. W., and Ford, K. L., 2000, The detection of potassic alteration by gamma-ray spectrometry—Recognition of alteration related to mineralization: *Geophysics*, **65**, 2001–2011.
- Ward, S. H., 1967, Electromagnetic theory for geophysical applications, in Ward, S. H., Ed., *Mining geophysics*, **2**, Theory: Soc. Expl. Geophys., 13–196.
- Ward, S. H., and Hohmann, G. W., 1988, Electromagnetic theory for geophysical applications, in Nabighian, M. N., Ed., *Electromagnetic methods in applied geophysics*, **1**, Theory: Soc. Expl. Geophys., 130–311.
- Zhang, Z., and Oldenburg, D. W., 1997, Recovering magnetic susceptibility from electromagnetic data over a one-dimensional earth: *Geophys. J. Internat.*, **130**, 422–434.
- 1999, Simultaneous reconstruction of 1-D susceptibility and conductivity from electromagnetic data: *Geophysics*, **64**, 33–47.